scientific reports

Check for updates

OPEN

Long-term variability of extreme precipitation with WRF model at a complex terrain River Basin

Yinchi Zhang[1,2,3], Chao Deng[1,2,3], Wanling Xu[13], Yao Zhuang[4,5,6], Lizhi Jiang[5], Caiying Jiang[7], Xiaojun Guan[5], Jianhui Wei[8], Miaomiao Ma[9], Ying Chen[1,2,3,12], Jian Peng[10,11] & Lu Gao[1,2,3,12] ✉

Global warming has profound effects on precipitation patterns, leading to more frequent and extreme precipitation events over the world. These changes pose significant challenges to the sustainable development of socio-economic and ecological environments. This study evaluated the performance of the new generation of the mesoscale Weather Research and Forecasting (WRF) model in simulating long-term extreme precipitation events over the Minjiang River Basin (MRB) of China from 1981 to 2020. We calculated 12 extreme precipitation indices from the WRF simulations and compared them with observations. The spatio-temporal variations of extreme precipitation were further analyzed in terms of intensity, frequency, and duration. The results indicated that the WRF model can appropriately reproduce the spatial distribution of extreme precipitation indices with acceptable biases. The performance is significantly better for intensity and frequency indices compared to duration indices. Except for PRCPTOT and R10mm, WRF accurately captures the interannual variations of extreme precipitation. Meanwhile, the results of the pre-whitening Mann-Kendall (PWMK) test suggested that WRF can identify significant increasing trends in extreme precipitation, particularly for R95p, R99p, and R50mm. This study provides valuable insights for extreme precipitation forecasting and warning in other mountainous regions.

Keywords Dynamical downscaling, WRF, Extreme precipitation, Spatio-temporal variations, Minjiang River Basin

The sixth assessment report of the Intergovernmental Panel on Climate Change (IPCC) demonstrates that the global surface temperature has warmed by 1.1℃ from 2011 to 2020 compared to the period from 1850 to 1900[1]. In the context of global warming, human activities lead to a significant increase in the frequency and intensity of extreme weather and climate events. The losses and damages inflicted on both natural and social systems far exceed the variability of natural climate[2–4]. Climate warming is also accompanied by the enhancement of hydrological cycle, manifested by the increase of both total precipitation and extreme precipitation worldwide[5,6]. The changes in precipitation variability will affect the climate resilience of social and ecological systems, which is an important issue that must be considered in the response to climate change[7]. It is forecasted that the enhanced hydrological cycle caused by global warming will lead to more extreme intra-annual precipitation patterns, characterized by stronger precipitation events and longer intervals between events[8]. Zhang et al. pointed out that the extreme precipitation in the global monsoon regions has shown an increasing trend in the past century, with a significant increasement in the contrast between wet and dry seasons[9]. Different combinations of precipitation mean state and variability will cause various types of hydrological, agricultural and ecological impacts in different

[1]Key Laboratory for Humid Subtropical Eco-geographical Processes of the Ministry of Education, Fujian Normal University, Fuzhou 350117, China. [2]Institute of Geography, Fujian Normal University, Fuzhou 350117, China. [3]College of Geographical Science, Fujian Normal University, Fuzhou 350117, China. [4]Fujian Meteorological Observatory, Fuzhou 350001, China. [5]Fujian Key Laboratory of Severe Weather, Fuzhou 350001, China. [6]Key Laboratory of Straits Severe Weather, China Meteorological Administration, Fuzhou 350001, China. [7]Nanping meteorological bureau of Fujian Province, Nanping 353000, China. [8]Institute of Meteorology and Climate Research, Karlsruhe Institute of Technology, 82439 Garmisch- Partenkirchen, Germany. [9]China Institute of Water Resources and Hydropower Research, Beijing 100038, China. [10]Department of Remote Sensing, Helmholtz Centre for Environmental Research-UFZ, Permoserstrasse 15, 04318 Leipzig, Germany. [11]Remote Sensing Centre for Earth System Research, Leipzig University, Talstr.35, 04103 Leipzig, Germany. [12]Fujian Provincial Engineering Research Center for Monitoring and Accessing Terrestrial Disasters, Fujian Normal University, Fuzhou 350117, China. [13]School of Ocean and Earth Science, Tongji University, Shanghai 200092, China. ✉email: l.gao@foxmail.com

regions, exacerbating the pressure on regional infrastructure design and water resources management[10–13]. In recent decades, the frequency and intensity of extreme precipitation in China have significantly increased, particularly in southeastern and northwestern China[14–16]. The Minjiang River Basin (MRB), located in the southeastern coastal region of China (Fig. 1a), experiences frequent extreme precipitation events due to its complex terrain and climate characteristics. Under the combined influences of weather system and topographic condition, extreme precipitation often triggers natural disasters such as floods, landslides, and debris flows, causing huge casualties and economic losses[17,18].

Global Climate Models (GCMs) are widely used to study climate change on a global scale, encompassing past, present, and future climate scenarios. While GCMs can capture large-scale circulation features, their performance in characterizing extreme precipitation on regional scales is less than ideal, primarily due to low horizontal resolution and simplified physical parameters[19]. In recent years, Regional Climate Models (RCMs) have experienced rapid development. RCMs use the outputs from GCMs as lateral boundary conditions and employ dynamical downscaling to obtain more refined information[20,21]. RCMs can accurately describe small and medium-scale circulation and surface features, and effectively capture the local forcing, thus reflecting more complex physical processes[22]. Numerous studies indicated that increasing the resolution of climate models can significantly enhance the performance[23–25]. Seth and Giorgi were the first to use RCMs to simulate extreme climate events, analyzing the circulation mechanisms of droughts and floods in the central United States[26]. Subsequently, the research work on simulating and predicting extreme precipitation based on RCMs has been carried out[27–31]. Goubanova and Li studied the potential changes of extreme precipitation events around the Mediterranean Basin based on the Laboratoire de Météorologie Dynamique Zoom (LMDZ) model, and implied that the total precipitation would decrease[32]. Moreover, Coppola et al. and Nishant et al. also used different RCMs to study extreme precipitation events on small and medium-scales[33,34]. The results verified that RCMs have strong feasibility to simulate extreme precipitation events.

As a new generation of mesoscale numerical weather prediction model, the Weather Research and Forecasting model (WRF) is equipped with a comprehensive dynamical framework and physical parameterization schemes, which describes the land-atmosphere coupling processes in detail with higher spatial and temporal resolution. The WRF model designed to meet the needs of atmospheric research and operational forecasting has been widely adopted by many countries and organizations[35,36]. Bao et al. used the WRF model to assess the current and future precipitation changes in China[37]. It is considered that the WRF model can well describe the annual cycle and frequency of precipitation intensity and is also reliable for the spatial distribution of total precipitation and extreme precipitation. Yang et al., Gao et al. and Deng et al. employed the WRF model for ensemble forecasting of extreme precipitation events in different regions of China, respectively, revealing its applicability and potential in capturing extreme precipitation[38–40]. Toride et al. reproduced the extreme precipitation changes based on the WRF model in the Shasta Dam watershed of the United States over during 1851–2010[10]. They discussed the impacts of changes in the intensity of extreme precipitation events on water resource management and
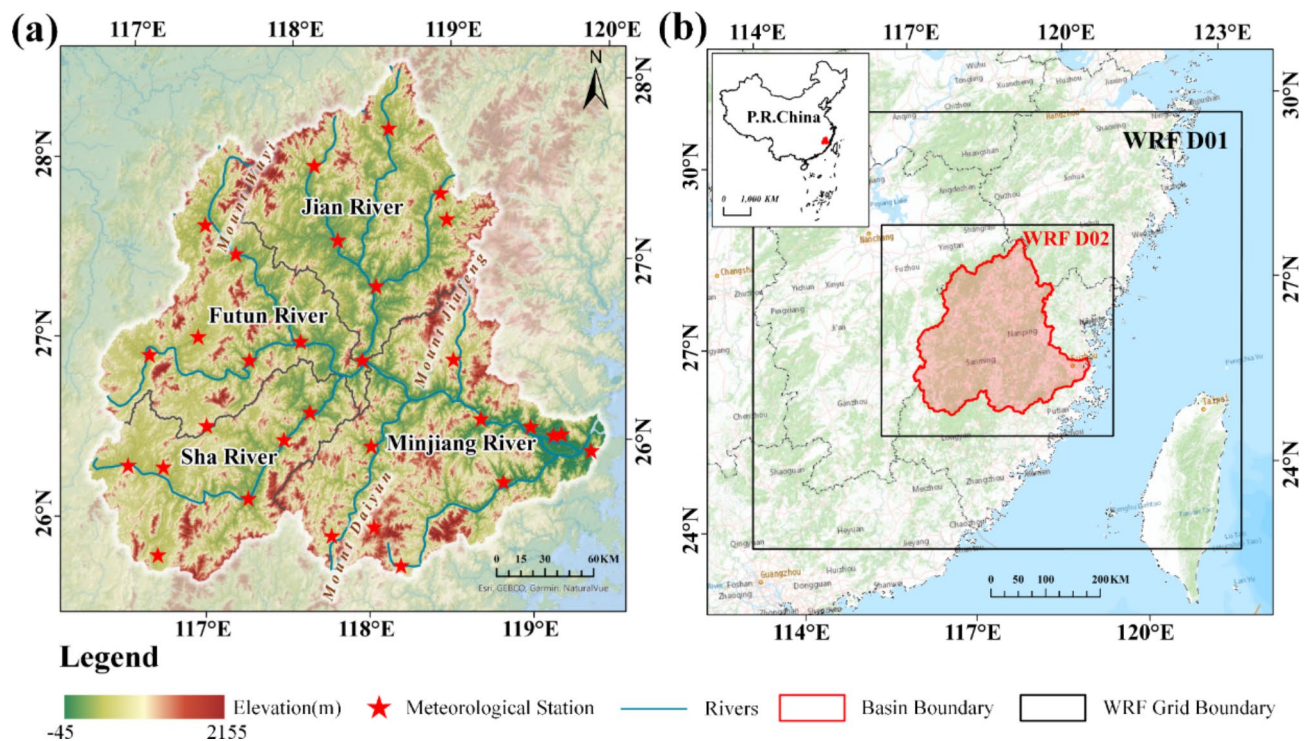

Fig. 1. Location of the study area (**a**) topographic features of the MRB. (**b**) WRF computational domain (D01-9 km, D02-3 km). The maps were created using ArcGIS Pro 3.0 software (https://www.esri.com/en-us/arcgis/products/arcgis-pro/overview).

sustainable development, emphasizing the importance of analyzing extreme precipitation trends on watershed scale.

Assessing the long-term trends of extreme precipitation in mountainous watersheds is crucial for understanding and mitigating the adverse impacts of natural disasters, particularly in regions where water resource management is heavily influenced by extreme weather events. Understanding these trends not only provides insights into the changing climate but also supports the development of effective disaster risk management strategies. Despite the importance of this issue, there is a notable gap in the current body of research. Studies that focus on the temporal and spatial variation of extreme precipitation in basins with complex topography are limited, especially when it comes to long-term simulations using high-resolution models like the WRF model. Most existing studies either focus on short-term simulations or regions with simpler topographic features, leaving a critical need for more detailed investigations in these challenging environments. This study aims to address this gap by conducting a comprehensive analysis of the spatio-temporal distribution and evolution patterns of extreme precipitation in the Minjiang River Basin (MRB) over the past 40 years. By utilizing high-resolution simulations, we aim to assess the model's capability in capturing extreme precipitation events and to gain a deeper understanding of the physical processes driving these trends. Ultimately, this study will contribute to the scientific understanding of extreme precipitation dynamics in complex terrains and the practical application of climate models in disaster risk reduction and water resource management.

Data and methods
Model and experimental design
WRF version 4.3 was used in this study[41]. The simulations were integrated from January 1, 1981 to December 31, 2020. The first grid has a resolution of 9 km with a grid size of 100×90, while the second grid has a resolution of 3 km with a grid size of 142×130 (Fig. 1b). Meanwhile, the model was configured with 45 vertical levels and time step was set at 30s. There are numerous physical parameterization schemes available for the WRF model, and there is no optimal scheme combination that can be applied to all regions or events because of the different climate and underlying surface conditions in each region. As a result, based on previous sensitivity experiments in the MRB[42], this study adopted the following parameterization schemes: New Tiedtke cumulus parameterization[43], Purdue Lin microphysical scheme[44], Dudhia shortwave radiation scheme[45], Rapid Radiative Transfer Model longwave radiation scheme[46], Noah land surface model[47]. In addition, when the model resolution is sufficiently high, certain convective processes can be explicitly represented[48]. Therefore, the cumulus scheme for the second grid was disabled. Many studies have indicated that land use and cover changes (LUCC) considerably influence the performance of the WRF model[49–51]. Hence, in order to ensure the accuracy of the results, this study replaced the LUCC data every ten years. The LUCC data were sourced from National Tibetan Plateau Data Center (http://data.tpdc.ac.cn/), with a spatial resolution reaching 100 m (Supplementary Figure S1).

Data
The initial and lateral boundary conditions of the WRF model were driven by the fifth-generation atmospheric reanalysis data (ERA5) from the European Centre for Medium-Range Weather Forecasts (ECWMF). ERA5 is available on regular latitude-longitude grids at $0.25° \times 0.25°$ resolution, with atmospheric parameters on 37 pressure levels. Compared with other reanalysis products, ERA5 has a more advanced 4DVAR assimilation system and higher spatio-temporal resolution[52].

There are 30 meteorological stations conducting long-term consecutive measurements in the MRB (Supplementary Table S1). These data are used to analyze the spatio-temporal characteristics of extreme precipitation and to evaluate the performance of the WRF model. The selected stations adequately capture precipitation trends and exhibit no continuous interruptions of two weeks or more. Additionally, to ensure the authenticity and accuracy of the data, an error analysis and quality control were conducted on all datasets.

Methods
Extreme precipitation indices
The Extreme Precipitation indices are commonly used to assess extreme precipitation events[53–55]. The 12 extreme precipitation indices used in this study are sourced from the Expert Team on Climate Change Detection Monitoring and Indices (ETCCDMI). In order to accurately assess the extreme precipitation characteristics in the study area, this research modifies Rnnmm as both R1mm and R50mm (Supplementary Table S2).

According to different classification criteria, extreme precipitation indices can be divided into various ways. For example, Alexander et al. classified them based on different time scales into monthly extreme indices and annual extreme indices, and based on different thresholds, they can also be divided into absolute threshold indices and relative threshold indices[56]. Irannezhad et al. classified extreme precipitation indices into four categories: annual precipitation amount, intensity, frequency, and duration[57]. Considering the extreme precipitation characteristics in the MRB, this research categorizes extreme precipitation indices into three classes: (1) Intensity indices, including PRCPTOT, SDII, RX1day, RX5day, R95p, and R99p. (2) Frequency indices, including R1mm, R10mm, R20mm, R50mm. (3) Duration indices, including CWD and CDD.

Trend analysis
The Mann-Kendall (MK) trend test is widely used non-parametric statistical method in the field of hydrometeorology. However, the autocorrelation of hydrological and meteorological elements often makes certain variables with insignificant trend to become significant. Yue and Wang proposed the addition of pre-whitening processing before the MK test to enhance the reliability of the series trend[58]. Many studies indicated that the pre-whitening Mann-Kendall (PWMK) trend test is more reasonable than the MK trend test[59–61]. It provides a more accurate description of trend changes in hydrometeorological elements such as temperature,

precipitation, and runoff. In this study, the PWMK trend test was used to calculate the trend changes in the extreme precipitation indices for both observational data and WRF model grid data. The pre-whitening procedure was applied by the following steps:

First, eliminating the linear trend of raw series.

$$Y_t = X_t - \beta_t \tag{1}$$

where Y_t, X_t and β_t are the de-trended series, raw series value, and linear regression slope of the trend in the raw series at time t, respectively.

Second, removing the autocorrelation term from the de-trended series.

$$Y_t^1 = Y_t - R_1 Y_{t-1} \tag{2}$$

where R_1 is the lag-1 serial correlation coefficient of the de-trended series and Y_t^1 is the de-trended and pre-whitened series, called the residual series.

Finally, we added the linear trend that was eliminated in the first step back to the de-trended or residual series.

$$Y_t^2 = Y_t^1 + \beta_t \tag{3}$$

where Y_t^2 is the pre-whitening series.

Evaluation criteria
To quantitatively validate the ability of the WRF model, this study selected correlation coefficient (CC), Kling-Gupta efficiency (KGE), and percent bias (PBIAS) to evaluate the goodness of fit. Additionally, CC and root mean square error (RMSE) were chosen to assess the spatial average bias between observed and simulated data (Table 1).

Results
Spatial distribution of extreme precipitation indices
Figure 2 illustrates the spatial distribution of observed and simulated extreme precipitation intensity indices in the MRB from 1981 to 2020. The observed annual total precipitation (OBS-PRCPTOT) decreases from northwestern to southeastern MRB, showing a significant gradient. The highest value, exceeding 1900 mm, is located at the junction of the Jianxi and Futun River Basins, while the lowest is less than 1600 mm in the downstream area. WRF-PRCPTOT and OBS-PRCPTOT exhibit good spatial consistency, but WRF overestimates precipitation, especially in the Jianxi and Shaxi River Basins, with maximum biases of 200–300 mm. On the contrary, WRF underestimates PRCPTOT in the downstream, with the minimum value of less than 1200 mm, and the biases ranging from 0~300 mm. The observed daily precipitation intensity (OBS-SDII) also shows a trend of transitioning from high values in the northwest to low values in the southeast. However, the difference is that the distribution range of the high value area of OBS-SDII is relatively small. WRF overestimates SDII, especially in the Shaxi River Basin and downstream MRB, where the maximum bias exceeds 3.5 mm·day⁻¹. The spatial distribution of observed maximum 1-day (OBS-RX1day) and 5-day (OBS-RX5day) precipitation is similar, with high values mainly along Mount Wuyi. OBS-RX1day ranges from 120 to 140 mm, and OBS-RX5day ranges from 220 to 265 mm. In comparison, the high value areas of WRF-RX1day and WRF-RX5day are more widely distributed and stronger. The biases are mainly concentrated in the northern of the Futunxi River Basin, the southern of the Shaxi River Basin and the downstream of the MRB, with the maximum bias exceeding 20 mm and 60 mm, respectively. Moreover, the high values of observed heavy precipitation (OBS-R95p) and extreme heavy precipitation (OBS-R99p) are both predominantly located near the Mount Wuyi, with values exceeding 900 mm and 325 mm, respectively. In comparison, WRF-R95p and WRF-R99p are significantly overestimated,

Metric	Formula	Optimal value	Range
CC	$CC = \dfrac{\sum_{i=1}^{n}(O_i-\overline{O_i})(M_i-\overline{M_i})}{\sqrt{\sum_{i=1}^{n}(O_i-\overline{O_i})^2}\sqrt{\sum_{i=1}^{n}(M_i-\overline{M_i})^2}}$	1	(0, 1)
NSE	$NSE = 1 - \dfrac{\sum_{t=1}^{T}(O_i^t-M_i^t)^2}{\sum_{t=1}^{T}(O_i^t-\overline{O_i})^2}$	1	(-∞, 1)
KGE	$KGE = 1 - \sqrt{(\alpha-1)^2 + (\beta-1)^2 + (\gamma-1)^2}$	1	(-∞, 1)
Pbias	$Pbias = \sum_{i=1}^{n}\dfrac{M_i-O_i}{O_i}$	0	(-∞, +∞)
RMSE	$RMSE = \sqrt{\dfrac{1}{n}\sum_{i=1}^{n}(M_i-O_i)}$	0	(0, +∞)

Table 1. Definition of evaluation criteria. Where O_i presents hydrometeorological data at the i station, M_i presents data at the WRF grid point closest to the i station, n is the numbers of stations, t presents the value of a specific moment in time, α presents the correlation coefficient, β presents the ratio of the mean of M_i to O_i, γ presents the ratio of the variance of M_i to O_i.
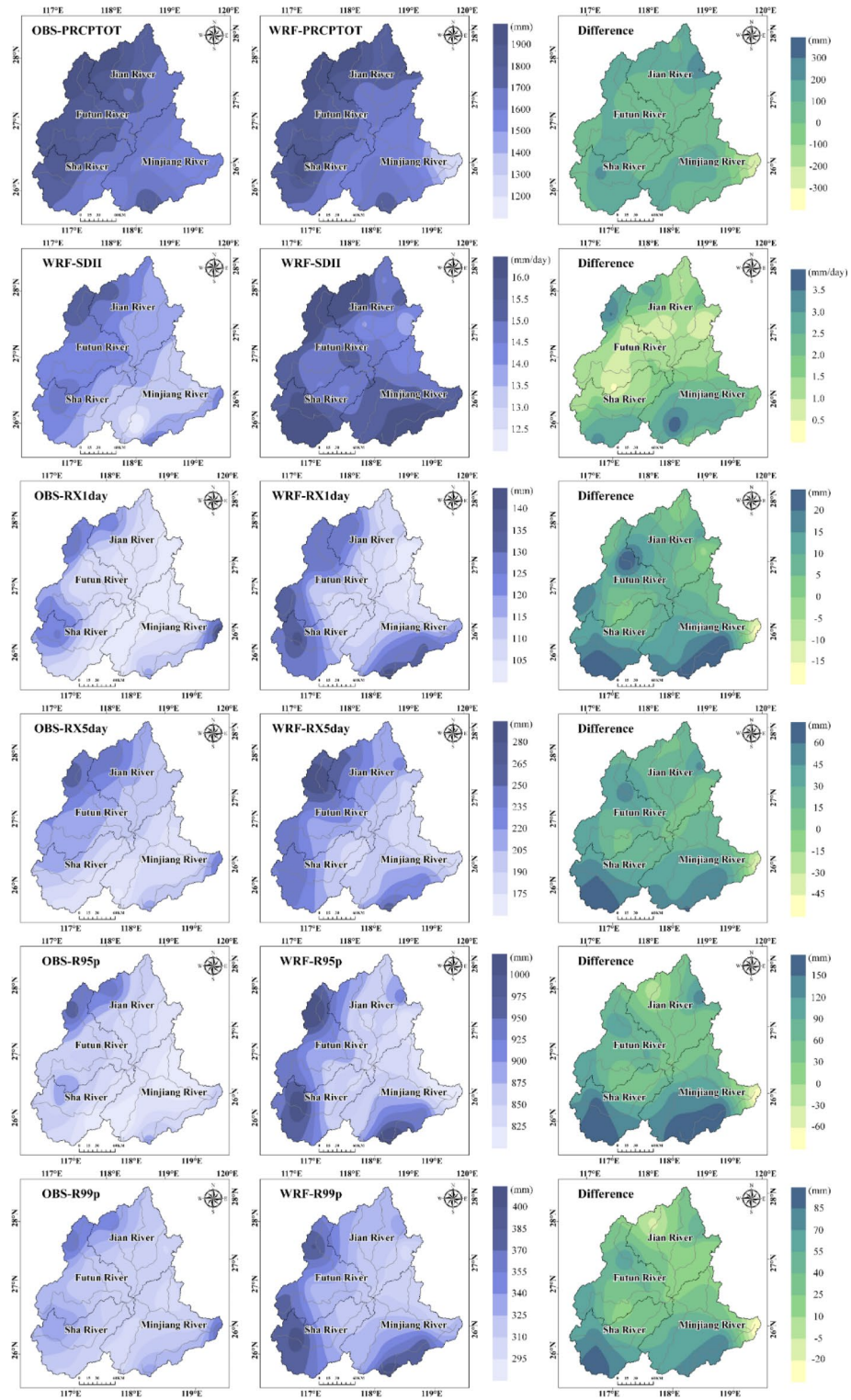
Fig. 2. Spatial distribution of extreme precipitation intensity indices from observations and WRF, as well as the biases over the MRB during 1981–2020.

with biases exceeding 120 mm and 70 mm, respectively, mainly distributed in the mountainous areas of Shaxi River Basin and the downstream of the MRB.

Overall, the extreme precipitation intensity gradually weakens from northwest to southeast, with high values mainly concentrated along Mount Wuyi. Meanwhile, WRF can capture the distribution of extreme precipitation intensity, but overestimates the value and extent of extreme precipitation, with the biases mainly distributed in the Shaxi basin and the complex mountainous areas of the downstream of the MRB (Mount Daiyun). The MRB

is located in the coastal monsoon region of southeastern China, characterized by significant climate variability. The enhanced frontal precipitation in this area is attributed to the overestimation of the simulated low-level subtropical high pressure and the westerly trough, or due to a systemic bias of sea-land thermal difference[62]. Many research findings also confirmed that WRF generally overestimates the extreme precipitation intensity in the southeastern region of China[39,63]. Notably, WRF underestimates extreme precipitation in the estuarine areas, which contrasts with other basin regions.

The extreme precipitation frequency and duration indices are illustrated in Fig. 3 The wet days (OBS-R1mm) in the basin generally exceeds 100 days, with a high value center located in the downstream of the MRB, ranging between 130 and 160 days. However, WRF generally underestimates R1mm, with a smaller bias in the northern ranging from −2 to 4 days, and a larger bias in the southern ranging from −14 to −32 days. Moreover, WRF underestimates R1mm, with biases ranging from −2 to 4 days in the north and −14 to −32 days in the south. The distribution of heavy precipitation days (OBS-R10mm) is similar to R1mm, with most areas exceeding 50 days (40–65 days). The distribution of very heavy precipitation days (OBS-R20mm) shows high values in the west near Mount Wuyi (28–34 days). WRF-R20mm generally follows the same pattern but has biases of 3–6 days in the western Jianxi River Basin. Additionally, The observed extreme heavy precipitation days (OBS-R50mm) are concentrated near Mount Wuyi, with values exceeding 7 days, while WRF overestimates R50mm in the Shaxi River Basin and MRB downstream, with biases ranging from 2.4 to 3.0 days.

The observed consecutive wet days (OBS-CWD) generally exceed 8 days, and the highest value appears in the downstream of the MRB, more than 10 days, showing a distribution pattern of high values in the northwest and low values in the southeast. On the contrary, WRF-CWD gradually decreases from north to south, with high values appearing in the northern of the Jianxi River Basin, ranging from 10 to 11 days, and low values areas occurring in the MRB estuary, ranging from 5 to 6 days. The observed consecutive dry days (OBS-CDD) exhibit a spatial characteristic of low values in the north and high values in the south, ranging from 25 to 37 days. However, WRF overestimates CDD, with biases mainly concentrated in the downstream of the MRB, exceeding 14 days in maximum.

In summary, extreme precipitation in the MRB shows a spatial correlation, with high values concentrated along Mount Wuyi. Meanwhile, as the extreme precipitation intensity increases, WRF gradually transitions from underestimating to overestimating for the extreme precipitation frequency. Among them, the spatial distribution of WRF-20 mm is the most consistent with the reality. However, for duration indices, WRF exhibits large spatial biases, likely due to the nonlinear dynamics in complex terrains, which challenge the simulation of continuous wet and dry conditions[64,65].

Taylor diagrams are presented in Supplementary Figure S2 to evaluates the performance of WRF for the extreme precipitation intensity, frequency, and duration. For intensity, PRCPTOT has the highest CC (0.90) and lowest RMSE (0.61), while SDII has the lowest CC (0.30) and highest RMSE (1.63). This indicates that WRF performs well for annual total precipitation but poorly for daily precipitation intensity. Among frequency indices, R20mm has the best performance (CC = 0.89, RMSE = 0.57), while R1mm and R50mm have CCs below 0.70. This suggests WRF overestimates extreme heavy precipitation while performing better for moderate and heavy rain. For CWD and CDD, WRF struggles with spatial distribution, showing low CC (0.52 and 0.42) and high RMSE (1.62 and 1.75).

Temporal variability of extreme precipitation indices

Figure 4; Table 2 illustrate the interannual variations and linear trends of the observed and simulated extreme precipitation indices in the MRB from 1981 to 2020. During this period, all the observed extreme precipitation intensity indices show an increasing trend. The correlation between the observed and simulated PRCPTOT is the strongest (CC of 0.97, KGE of 0.85), and the bias is the smallest (PBIAS of −1.45%), indicating that WRF can effectively capture the interannual variations of PRCPTOT. The observed PRCPTOT has a positive trend of 31.83 mm·10years^{-1}, while the WRF results show a negative trend of −32.46 mm·10years^{-1}. For SDII, the trends of observations and simulations are 0.37 mm·day^{-1}·10years^{-1} and 0.44 mm·day^{-1}·10years^{-1}, respectively, showing good consistency in the time series (CC of 0.85, KGE of 0.80, PBIAS of 9.58%). The observed RX1day and RX5day show the same positive trend, with 3.92 mm·10years^{-1} and 2.45 mm·10years^{-1}, respectively. The simulated RX1day and RX5day are 4.93 mm·10years^{-1} and 7.58 mm·10years^{-1}, respectively. Compared with the observations, there are different degrees of overestimation, but CC and KGE are both around 0.8, showing a strong correlation. For R95p and R99p, the trend of simulations is highly consistent with that of the observations (CC > 0.85, KGE > 0.80). The observed and simulated R95p show a trend of increase with 25.63 mm·10years^{-1} and 28.35 mm·10years^{-1}, and for R99p, they are 11.06 mm·10years^{-1} and 14.57 mm·10years^{-1}, respectively. Overall, for the extreme precipitation intensity, WRF exhibits a good performance and strong correlation. In addition to PRCPTOT, the variation trends of simulated and observed intensity indices are consistent.

For the extreme precipitation frequency indices, the observations and simulations exhibit a high correlation, with CC mostly above 0.9 and KGE above 0.8. Specifically, R1mm of both observations and simulations show a decreasing trend, with −1.29 mm·10years^{-1} and −3.32 mm·10years^{-1}, respectively, indicating a strong correlation in the time series (CC of 0.93, KGE of 0.83, PBIAS of −9.70%). For R10mm, the WRF results are close to those of R1mm (CC of 0.92, KGE of 0.86, PBIAS of −6.29%), but the observations and simulations show a opposite trend, with 0.32 days·10years^{-1} and −1.13 days·10years^{-1}, respectively. The performance of R20mm closely matches the observations, with CC of 0.94 and PBIAS of only 6.47%. Additionally, the trend of simulated R20mm is 0.41 days·10years^{-1}, slightly lower than the observations of 0.54 days·10years^{-1}. The correlation of R50mm is the lowest (CC of 0.89, KGE of 0.78), with the largest bias (PBIAS of 15.86%), but the trend is very close to observations, with 0.59 days·10years^{-1} and at 0.54 days·10years^{-1}, respectively.

Both CWD and CDD show decreasing trends, with −0.22 days·10years^{-1} and −0.34 days·10years^{-1}, respectively. The WRF results show similar declining trends, with −0.15 days·10years^{-1} for CWD and −0.23
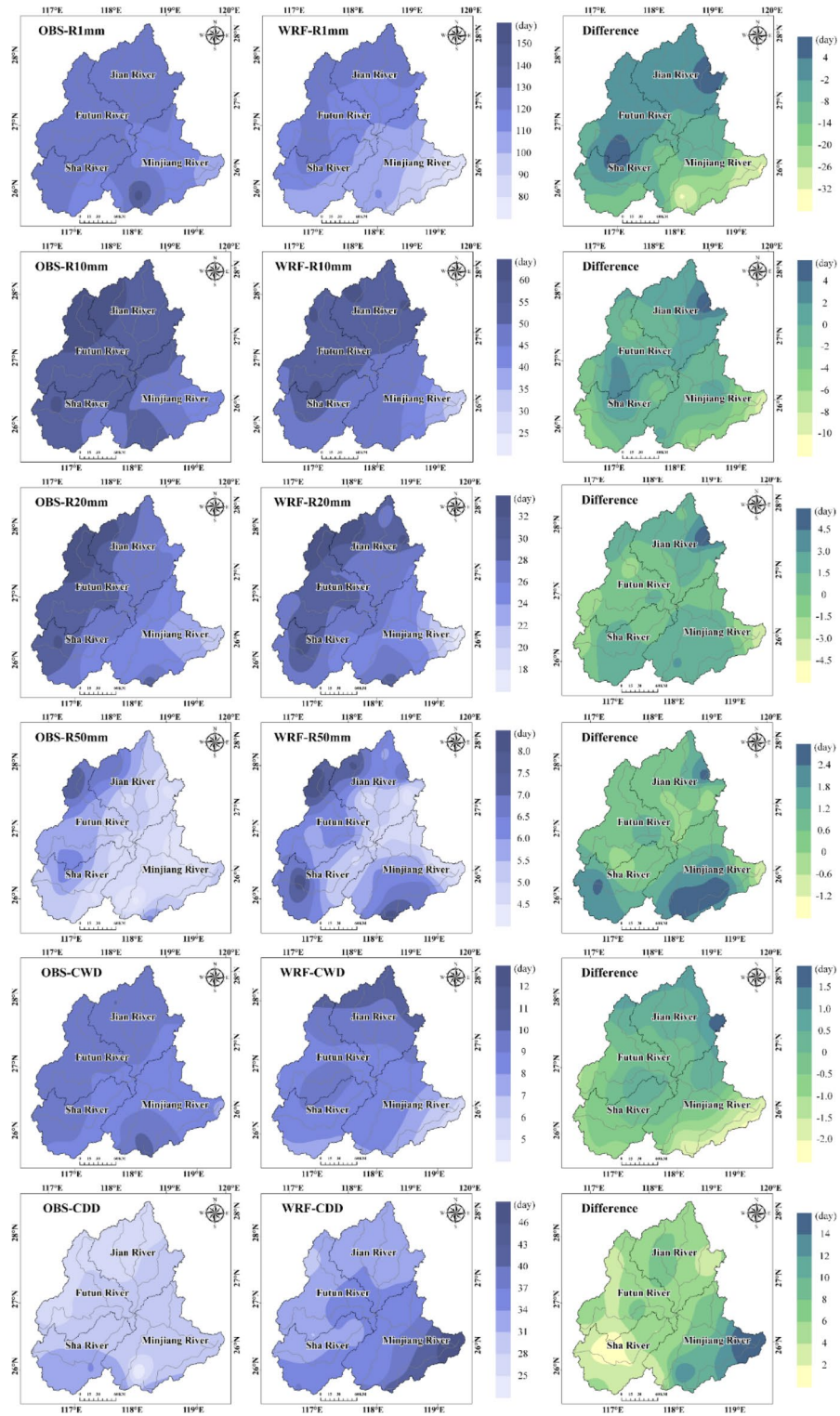
Fig. 3. As in Fig. 2 but for extreme precipitation frequency and duration indices.

days·10years⁻¹ for CDD. CDD shows higher temporal correlation (CC = 0.86, KGE = 0.65) but a larger bias (PBIAS = −20.74%). In conclusion, WRF generally captures the interannual variations of all extreme precipitation indices in the MRB, with CC mostly above 0.80. Except for PRCPTOT and R10mm, WRF also accurately describes the trends of each index. In comparison, WRF tends to overestimate the variation rates of the extreme precipitation intensity indices (except PRCPTOT), while the extreme precipitation frequency (except R50mm) and duration indices exhibit the opposite trend.
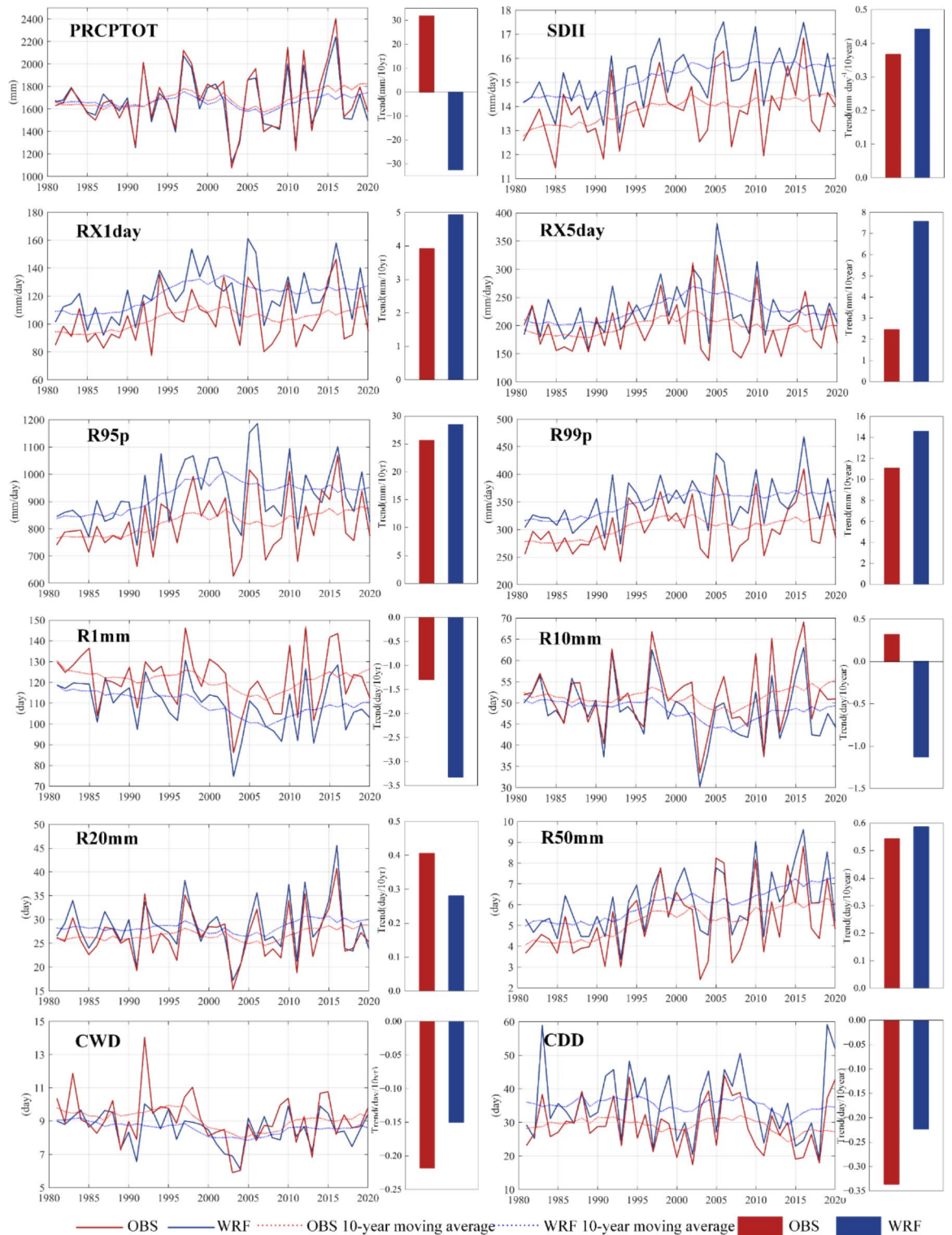
Fig. 4. Interannual variation (left) and temporal linear trend (right) of extreme precipitation indices over the MRB during 1981–2020.

Spatio-temporal evolution of extreme precipitation indices

Figures 5 and 6 show the PWMK trends of 12 extreme precipitation indices in the MRB from 1981 to 2020. For the intensity indices, OBS-PRCPTOT generally shows an increasing trend, with only 5 stations exhibiting a decreasing trend, mainly distributed in the downstream. WRF-PRCPTOT closely matches OBS-PRCPTOT in the northern MRB but shows overestimation and underestimation in the downstream. OBS-SDII exhibits an increasing trend across the basin, with seven stations reaching a 0.05 significance level, mainly in the

Category	Index	CC	KGE	PBIAS	Variation rate
Intensity	PRCPTOT	0.97	0.85	−1.45%	31.83/−32.46 (mm·10years^{-1})
	SDII	0.85	0.80	9.58%	0.37/0.44 (mm·day^{-1}·10year^{-1})
	RX1day	0.79	0.75	16.75%	3.92/4.93 (mm·10 years^{-1})
	RX5day	0.80	0.76	15.16%	2.45/7.58 (mm·10 years^{-1})
	R95p	0.85	0.80	16.75%	25.63/28.35 (mm·10 years^{-1})
	R99p	0.89	0.83	14.62%	11.06/14.57 (mm·10 years^{-1})
Frequency	R1mm	0.93	0.83	−9.70%	−1.29/−3.32 (mm·10 years^{-1})
	R10mm	0.92	0.86	−6.29%	0.32/−1.13 (mm·10 years^{-1})
	R20mm	0.94	0.89	6.47%	0.54/0.41 (mm·10 years^{-1})
	R50mm	0.89	0.78	15.86%	0.54/0.59 (mm·10 years^{-1})
Duration	CWD	0.74	0.42	−6.17%	−0.22/−0.15 (mm·10 years^{-1})
	CDD	0.86	0.65	−20.74%	−0.34/−0.23 (mm·10 years^{-1})

Table 2. The evaluation criteria and variation rate of the observation (left) and WRF (right).

northwestern MRB. WRF tends to overestimate SDII's trend, with nine stations showing significance at 0.05. OBS-RX1day shows a decreasing trend at only five stations, with others increasing. WRF generally overestimates this increasing trend, especially in the central MRB. OBS-RX5day displays an increasing trend in the north and south but a decreasing trend in the center. WRF overestimates the increase in RX5day, with five stations showing significance. OBS-R95p shows an increasing trend, except for Gutian, with Tai'ning reaching significance. WRF-R95p overestimates the trend in the northwestern MRB, but in the downstream, it shows a decreasing trend in three stations. Compared with the observations, the simulated R99p shows a slight overestimation in the north and west of the basin, but generally performs well.

For the frequency indices, OBS-R1mm generally shows a decreasing trend except for Changle. WRF-R1mm shows consistent decline but overestimates the rate in the south, with 15 stations significant at 0.05. OBS-R10mm shows increasing trends in the north and decreasing in the south, with 19 stations increasing and 11 decreasing. However, WRF-R10mm overestimates the southern decline, with 24 stations showing a decline and six reaching significance. OBS-R20mm shows a general increasing trend in the north and south, with no significant trend except at Guangze station. The WRF results are opposite to the observations in the Shaxi and the downstream of the MRB, with 4 stations showing a significant decreasing trend. OBS-R50mm shows an increasing trend throughout the basin, with Jian'ou and Mingxi stations reaching significance. Compared with the observations, WRF-R50mm overestimates the increase in the western basin, with six stations showing significance, while in the downstream, it shows a decreasing trend in three stations.

For the duration indices, OBS-CWD and OBS-CDD show a decreasing trend, with 2 and 1 stations reaching a significance level of 0.05, respectively. Meanwhile, WRF can simulate the decreasing trends of CWD and CDD across the entire basin, although with varying degrees of biases.

Supplementary Table S3 summarizes the PWMK trends of 12 extreme precipitation indices at each station. Among them, PRCPTOT, SDII, RX1day, R95p, R99p, and R50mm exhibit an increasing trend at over 20 stations. The trend of SDII is most pronounced across the entire basin, with 7 stations reaching a significance level of 0.05. On the contrary, R1mm, CWD, and CDD show a decreasing trend at over 20 stations, with approximately 97% of the stations showing a negative trend for R1mm among 30 stations. Among the 12 indices, the results of R95p, R99p, and R50mm are closest to the observations, with a hit rate of 0.73. However, the performance of RX5day and R10mm is the poorest, with a hit rate of only 0.43.

In summary, the intensity indices show an upward trend in the MRB during 1981–2020, especially in the northwestern and western areas near Mount Wuyi. As for the frequency indices, the spatio-temporal evolution varies across different values. Specifically, across the entire basin, R1mm exhibits a decreasing trend, while R50mm showed an increasing trend. Meanwhile, the frequency of high intensity precipitation (R20mm, R50mm) significantly increases in the northern and western mountainous areas. Overall, WRF captures the spatio-temporal evolution patterns of various extreme precipitation indices, though it overestimates the increasing trend of intensity indices in the western and northern mountains and overestimates the decreasing trend of low-intensity frequency indices in the southern basin.

Discussion

In this study, the extreme precipitation intensity and frequency indices in the MRB from 1981 to 2020 show a positive trend (except R1mm), while the duration indices exhibit a negative trend, indicating that the extreme and sudden precipitation in the region increased and the persistence decreased. These findings are consistent with previous research results in southeastern China[15,18,54].

We are particularly interested in the changes of extreme precipitation in small-scale complex terrain watersheds. The terrain in these areas is steep, and the confluence speed of rainstorm and flood is fast. It is easy to form a huge flood peak in a short time, which endangers the downstream urban plain area[66]. Overall, the WRF model generally shows wet biases in high-altitude areas like the Wuyi Mountains and dry biases in low-lying plains, such as the estuary region of the MRB. As precipitation intensity increases, the model shifts from underestimating to overestimating extreme events. For most extreme precipitation indices (SDII, RX1day, RX5day,
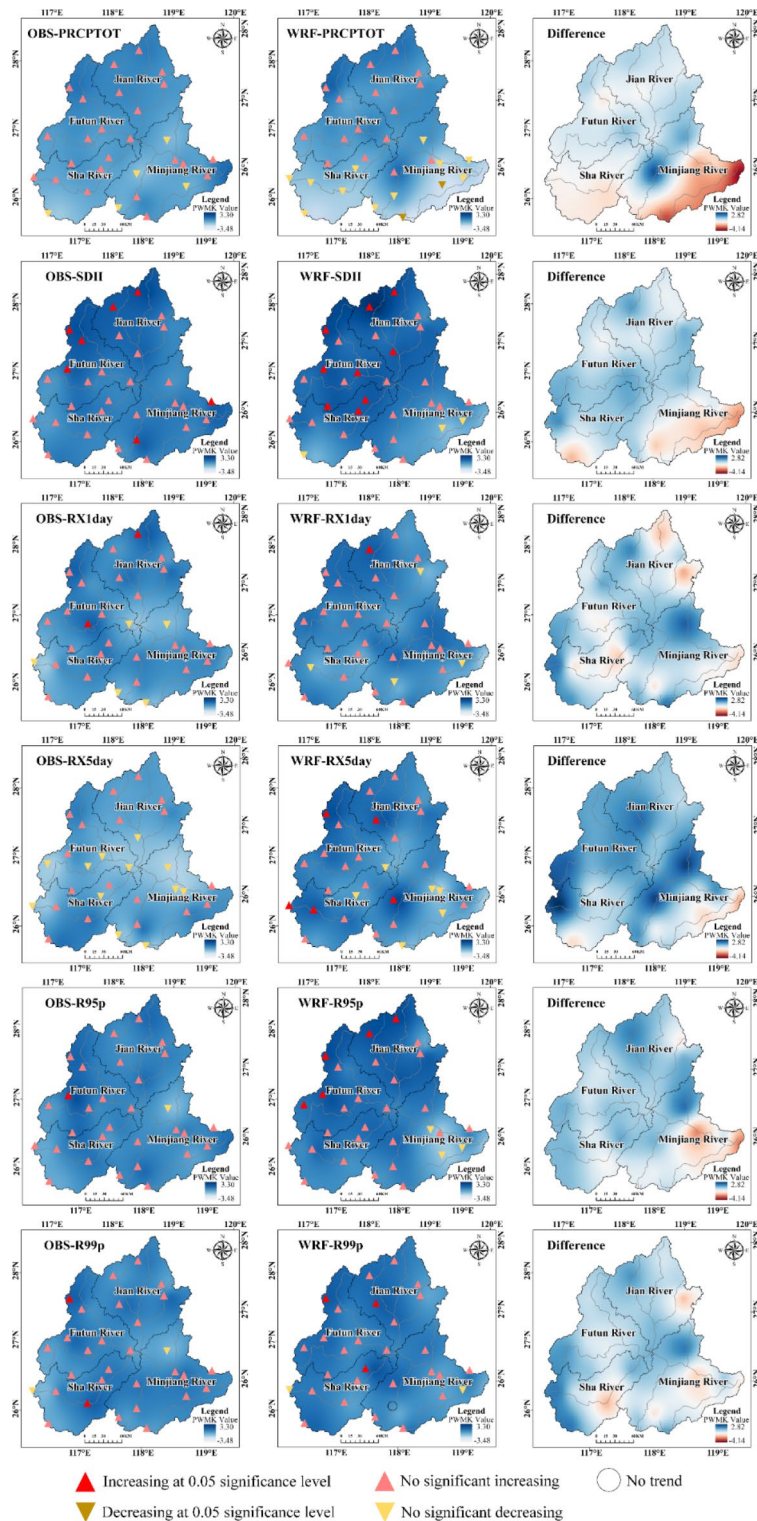
Fig. 5. Spatial distribution of the PWMK test for 12 extreme precipitation intensity indices in the MRB during 1981–2020.

R95p, R99p), overestimation occurs in mountainous regions, with high-intensity events (R50mm) following the same trend. Complex topographical features and the presence of intense weather systems pose significant challenges in the precise modeling of extreme precipitation events[67–69]. Compared to reality, the smoothing of complex terrain in the model may significantly reduce the terrain resistance encountered by air masses during ascent, weaken water vapor convergence at low altitudes, and result in excessive precipitation in mountainous areas[70,71]. Additionally, the simulation of evaporation and condensation processes in the WRF model may not be
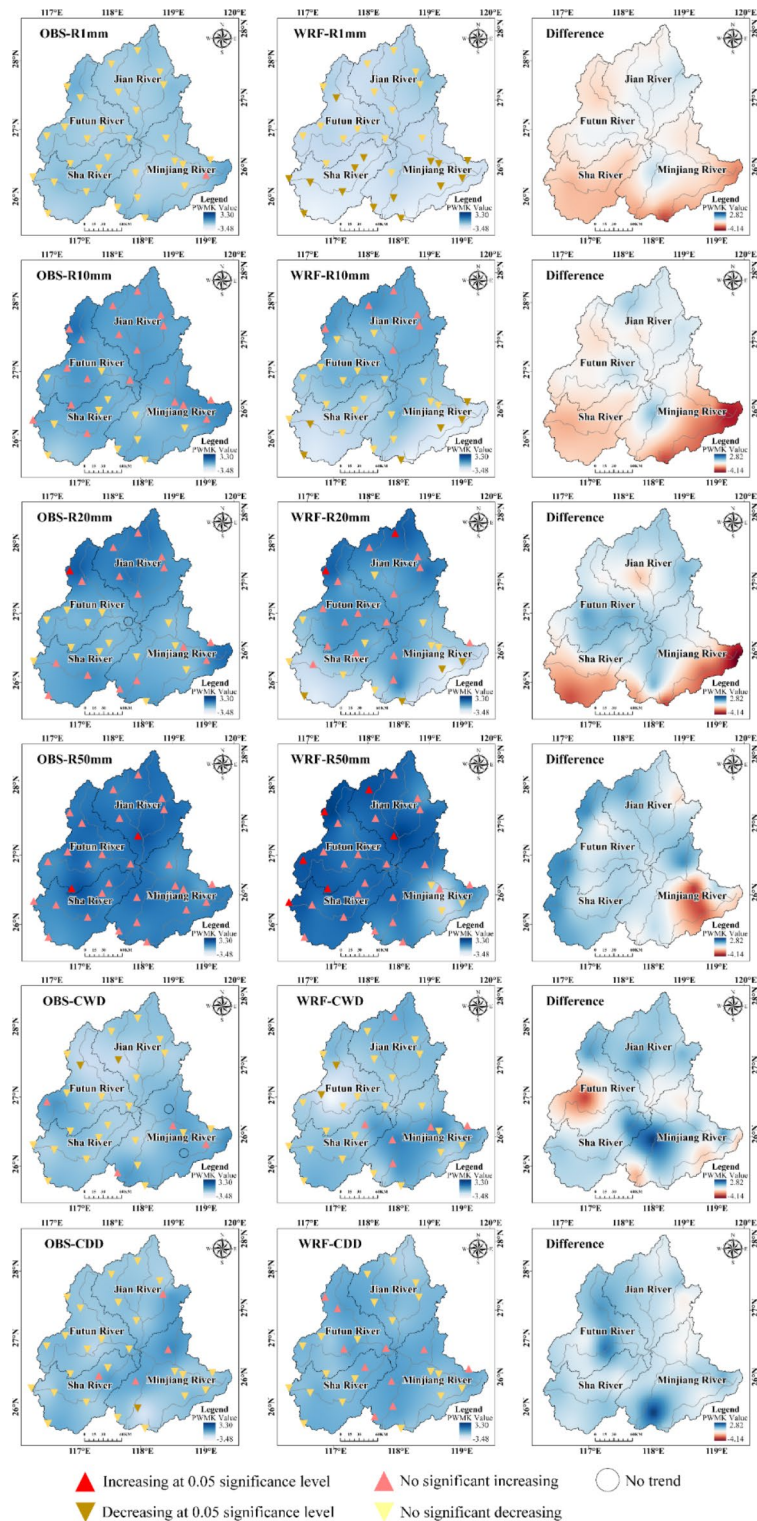
Fig. 6. As in Fig. 5 but for extreme precipitation frequency and duration indices.

entirely accurate, particularly in areas with strong terrain-induced uplift, which may lead to an overestimation of atmospheric water vapor[72]. Numerous studies and evidence indicate a close relationship between monsoon, tropical cyclones, and extreme precipitation events[73–77]. However, reconstructing extreme precipitation caused by severe weather processes based on RCMs still presents certain limitations and uncertainties. Mandal et al. found that the WRF model provided a reasonable prediction of the spatial distribution of tropical cyclone precipitation but overestimated the intensity in the core regions of heavy rainfall, this overestimation may be significantly influenced by the vertical wind shear in the initial conditions[78]. Yang et al. used the WRF model to

reconstruct East Asian summer monsoon precipitation and suggested that the overestimation of precipitation may further induce or amplify circulation biases at different scales, highlighting the critical role of precipitation feedback on the circulation and precipitation distribution[38]. The MRB has long been significantly impacted by the East Asian monsoon and tropical cyclones, the instantaneous and intense extreme precipitation events are mostly concentrated in the post-flood period (July to September) when the summer monsoon and tropical cyclones are active[79], which is undoubtedly an important reason for the unsatisfactory model results.

There are numerous physical parameterization schemes in the WRF model, and the microphysics (MP) and cumulus (CU) schemes have a particularly significant impact on the accuracy of precipitation simulations[80–83]. Although we conducted comprehensive sensitivity tests and optimizations on the model's MP (Purdue Lin microphysical scheme) and CU (New Tiedtke cumulus parameterization) schemes prior to this study to improve the accuracy of the simulation results, certain issues remain unavoidable because of the inherent limitations of each scheme. Nguyen-Xuan et al. found that New Tiedtke scheme over land produces excessive orographic precipitation, thus destroying its spatial pattern[84]. Compared to other CU schemes, the New Tiedtke scheme simulates significantly greater convective rainfall, with peak values notably higher than those of other schemes. Additionally, there is a certain deviation in the simulation of tropical cyclone positions using this scheme[85]. However, Xu et al. suggested that using the Purdue Lin scheme at a low resolution (3 km) constrains net condensation and moisture convergence, preventing accurate capture of localized weak convective precipitation[86]. This can provide a reference for explaining the model's underestimation of low intensity precipitation indices (R1mm, CWD). Moreover, Yang et al. believe that even with optimized parameters, circulation biases still exist because of inappropriate radiation or planetary boundary layer (PBL) processes in the model[36].

There is much evidence that more realistic land use data can improve simulation results[49,87,88]. It is worth emphasizing that although this study replaced the default land use data with high quality data closest to the study period, the simulated results still generally underestimated the extreme precipitation intensity and frequency in the estuarine area of the MRB, possibly due to the influences of urbanization processes (Supplementary Figure S1). Feng et al. suggested that changes of urban underlying surface characteristics not only directly affect urban temperature, but also have an important impact on precipitation[89]. Lin et al. found that urban land use changes significantly affect the atmospheric thermodynamic processes in the boundary layer, which ultimately change the spatio-temporal characteristics of precipitation[90]. Yang et al. proposed that urbanization enhances the thermal disturbance of temperature and surface pressure fields and strength the dynamic conditions during precipitation events[91]. For the WRF model, a spatial resolution of 3 km may not be sufficient to describe the complex microscale meteorological features within cities. Additionally, the processes such as atmospheric turbulence and radiation transfer within the urban areas may require more sophisticated parameterization schemes for accurate simulation[92].

In general, the WRF model shows some potential in simulating extreme precipitation in complex terrain regions, yet this study still reveals some shortcomings. Given the complexity of extreme precipitation related to terrain effects, weather systems, and radiation schemes, among other dynamic and physical processes, further efforts are required to enhance accuracy. For instance, addressing the quality of boundary conditions through techniques like data assimilation, and conducting coupled simulation focusing on hydrological processes, urban climate characteristics, and dynamic responses of ecosystems. Additionally, due to the limitation in computational resources, our simulation experiments only employed one RCM. Therefore, future research should incorporate multiple RCMs and employ optimal ensemble methods to obtain more extensive and reliable information on future changes in extreme precipitation, ultimately facilitating climate change impact assessments and adaptation services.

Conclusions

In this study, we used the WRF model to simulate the distribution and variation of extreme precipitation in the MRB during 1981–2020 based on four different land use and land covers. The extreme precipitation indices were calculated based on both observations and simulations. The performance of the WRF model was evaluated from three aspects: spatial distribution, temporal variability, and spatio-temporal evolution. The important conclusions drawn from this study are as follows.

1) Overall, WRF shows appropriate performance in capturing the spatial distribution of extreme precipitation indices. Among them, the results of extreme precipitation intensity and frequency indices are significantly better than that of duration indices, with the highest CC observed for PRCPTOT and R20mm, reaching 0.90 and 0.89, respectively. WRF generally overestimates the extreme precipitation intensity in the MRB, particularly in the complex mountainous regions of the Shaxi Basin and the downstream of the MRB, whereas it yields contrasting results for the flat terrain of the MRB estuary. For the extreme precipitation frequency, there is a certain relationship between the bias and the precipitation intensity, wherein high value events exhibit wet biases while low value events exhibit dry biases. Additionally, the results of CWD and CDD are relatively poor, with CC of only 0.52 and 0.42, respectively.

2) In terms of the temporal variability, WRF generally captures the interannual variation trends of the 12 extreme precipitation indices, with CC mostly exceeding 0.8. PRCPTOT exhibits the highest CC of 0.97, while CWD shows the lowest CC of only 0.74. Except for PRCPTOT and R10mm, the observed and simulated linear trends of other indices are consistent. Compared with the observations, WRF overestimates the variation rate in the extreme precipitation intensity indices and underestimates the variation rate in the extreme precipitation frequency and duration index.

3) WRF can basically reproduce the spatio-temporal evolution characteristics of extreme precipitation in the MRB. The results of the PWMK trend test show that the extreme precipitation intensity is on the rise, and WRF can capture the significant rising area. Across the entire basin, R1mm shows a gradual downward

trend, while R50mm shows a gradual upward trend, and the simulated results are more extreme. In addition, for CWD and CDD, the results of observations and simulations show a general trend of decline.

Data availability

References

1. IPCC. in *Climate Change 2023: Synthesis Report. Contribution of Working Groups I, II and III to the Sixth Assessment Report of the Intergovernmental Panel on Climate Change [Core Writing Team*. 35–115 (eds Lee, H. & Romero, J.) (IPCC, 2023). https://doi.org/10.59327/IPCC/AR6-9789291691647.
2. Contribution of Working Group III to the Sixth Assessment Report of the Intergovernmental Panel on Climate Change [P.R. in *Climate Change 2022: Mitigation of Climate Change*. (eds Shukla, J., Skea, R., Slade, A., Al Khourdajie, R., van Diemen, D., McCollum, M., Pathak, S., Some, P., Vyas, R., Fradera, M., Belkacemi, A., Hasija, G., Lisboa, S., Luz, J. & Malley) (Cambridge University Press, 2022). https://doi.org/10.1017/9781009157926.
3. Du, H. et al. Extreme Precipitation on Consecutive days occurs more often in a warming climate. *Bull. Amer Meteor. Soc.* **103**, E1130–E1145. https://doi.org/10.1175/BAMS-D-21-0140.1 (2022).
4. Ghanbari, M., Arabi, M., Georgescu, M. & Broadbent, A. M. The role of climate change and urban development on compound dry-hot extremes across US cities. *Nat. Commun.* **14**, 3509. https://doi.org/10.1038/s41467-023-39205-x (2023).
5. Hirpa, F. A. et al. Streamflow response to climate change in the Greater Horn of Africa. *Clim. Change.* **156**, 341–363. https://doi.org/10.1007/s10584-019-02547-x (2019).
6. Peng, J. et al. The impact of the Madden-Julian Oscillation on hydrological extremes. *J. Hydrol.* **571**, 142–149. https://doi.org/10.1016/j.jhydrol.2019.01.055 (2019).
7. Zhang, W. et al. Increasing precipitation variability on daily-to-multiyear time scales in a warmer world. *Sci. Adv.* **7**, eabf8021. https://doi.org/10.1126/sciadv.abf8021 (2021).
8. Knapp, A. K. et al. Consequences of more Extreme Precipitation regimes for Terrestrial ecosystems. *BioScience* **58**, 811–821. https://doi.org/10.1641/B580908 (2008).
9. Zhang, W., Zhou, T., Zhang, L. & Zou, L. Future intensification of the Water cycle with an enhanced Annual cycle over Global Land Monsoon regions. *J. Clim.* **32**, 5437–5452. https://doi.org/10.1175/JCLI-D-18-0628.1 (2019).
10. Toride, K., Cawthorne, D. L., Ishida, K., Kavvas, M. L. & Anderson, M. L. Long-term trend analysis on total and extreme precipitation over Shasta Dam watershed. *Sci. Total Environ.* **626**, 244–254. https://doi.org/10.1016/j.scitotenv.2018.01.004 (2018).
11. Ahmed, K., Shahid, S., Chung, E. S., Wang, X. & Harun, S. B. Climate change uncertainties in seasonal drought severity-area-frequency curves: case of arid region of Pakistan. *J. Hydrol.* **570**, 473–485. https://doi.org/10.1016/j.jhydrol.2019.01.019 (2019).
12. Kumar, N., Patel, P., Singh, S. & Goyal, M. K. Understanding non-stationarity of hydroclimatic extremes and resilience in Peninsular catchments, India. *Sci. Rep.* **13**, 12524. https://doi.org/10.1038/s41598-023-38771-w (2023).
13. Singh, S., Goyal, M. K. & Saikumar, E. Assessing Climate vulnerability of Ramsar wetlands through CMIP6 projections. *Water Resour. Manag.* **38**, 1381–1395. https://doi.org/10.1007/s11269-023-03726-3 (2024).
14. Xu, X., Du, Y., Tang, J. & Wang, Y. Variations of temperature and precipitation extremes in recent two decades over China. *Atmos. Res.* **101**, 143–154. https://doi.org/10.1016/j.atmosres.2011.02.003 (2011).
15. Fu, G. et al. Temporal variation of extreme rainfall events in China, 1961–2009. *J. Hydrol.* **487**, 48–59. https://doi.org/10.1016/j.jhydrol.2013.02.021 (2013).
16. Yuan, Z., Yang, Z., Yan, D. & Yin, J. Historical changes and future projection of extreme precipitation in China. *Theor. Appl. Climatol.* **127**, 393–407. https://doi.org/10.1007/s00704-015-1643-3 (2017).
17. Easterling, D. R. et al. Observed variability and Trends in Extreme Climate events: a brief review *. *Bull. Amer Meteor. Soc.* **81**, 417–425 (2000).
18. Tang, Y. et al. Drivers of Summer Extreme precipitation events over East China. *Geophys. Res. Lett.* **48** (e2021GL093670). https://doi.org/10.1029/2021GL093670 (2021).
19. Mahajan, S., Evans, K. J., Branstetter, M., Anantharaj, V. & Leifeld, J. K. Fidelity of Precipitation extremes in High Resolution Global Climate simulations. *Procedia Comput. Sci.* **51**, 2178–2187. https://doi.org/10.1016/j.procs.2015.05.492 (2015).
20. Rummukainen, M. State-of-the-art with regional climate models. *WIREs Clim. Change.* **1**, 82–96. https://doi.org/10.1002/wcc.8 (2010).
21. Gao, S., Zhu, S. & Yu, H. Dynamical downscaling of temperature extremes over China using the WRF model driven by different lateral boundary conditions. *Atmos. Res.* **278**, 106348. https://doi.org/10.1016/j.atmosres.2022.106348 (2022).
22. Giorgi, F. & Shields, C. Tests of precipitation parameterizations available in latest version of NCAR regional climate model (RegCM) over continental United States. *J. Geophys. Res. : Atmos.* **104**, 6353–6375. https://doi.org/10.1029/98JD01164 (1999).
23. Klavans, J. M., Poppick, A., Sun, S. & Moyer, E. J. The influence of model resolution on temperature variability. *Clim. Dyn.* **48**, 3035–3045. https://doi.org/10.1007/s00382-016-3249-6 (2017).
24. Armstrong, E., Hopcroft, P. O. & Valdes, P. J. Reassessing the value of Regional Climate modeling using Paleoclimate simulations. *Geophys. Res. Lett.* **46**, 12464–12475. https://doi.org/10.1029/2019GL085127 (2019).
25. Ingram, W. & Bushell, A. C. Sensitivity of Climate feedbacks to Vertical Resolution in a general circulation model. *Geophys. Res. Lett.* **48** https://doi.org/10.1029/2020GL092268 (2021). e2020GL092268.
26. Seth, A. & Giorgi, F. The effects of Domain Choice on Summer Precipitation Simulation and Sensitivity in a Regional Climate Model. *J. Clim.* **11**, 2698–2712 (1998).
27. Mishra, V., Dominguez, F. & Lettenmaier, D. P. Urban precipitation extremes: how reliable are regional climate models? Geophys. *Res. Lett.* **39**, 2011GL050658. https://doi.org/10.1029/2011GL050658 (2012).
28. Mishra, V. et al. Reliability of regional and global climate models to simulate precipitation extremes over India. *J. Geophys. Res. : Atmos.* **119**, 9301–9323. https://doi.org/10.1002/2014JD021636 (2014).
29. Lehtonen, I., Ruosteenoja, K. & Jylhä, K. Projected changes in European extreme precipitation indices on the basis of global and regional climate model ensembles. *Int. J. Climatol.* **34**, 1208–1222. https://doi.org/10.1002/joc.3758 (2014).
30. Thober, S. & Samaniego, L. Robust ensemble selection by multivariate evaluation of extreme precipitation and temperature characteristics. *J. Geophys. Res. : Atmos.* **119**, 594–613. https://doi.org/10.1002/2013JD020505 (2014).
31. Olmo, M. E. & Bettolli, M. L. Extreme daily precipitation in southern South America: statistical characterization and circulation types using observational datasets and regional climate models. *Clim. Dyn.* **57**, 895–916. https://doi.org/10.1007/s00382-021-05748-2 (2021).

32. Goubanova, K. & Li, L. Extremes in temperature and precipitation around the Mediterranean basin in an ensemble of future climate scenario simulations. *Global Planet. Change.* **57**, 27–42. https://doi.org/10.1016/j.gloplacha.2006.11.012 (2007).

33. Coppola, E. et al. Assessment of the European Climate Projections as Simulated by the Large EURO-CORDEX Regional and Global Climate Model Ensemble. J. Geophys. Res.: Atmos. 126, e (2021). https://doi.org/10.1029/2019JD032356.

34. Nishant, N. & Sherwood, S. C. How strongly are Mean and Extreme Precipitation coupled? Geophys. *Res. Lett.* **48** https://doi.org/10.1029/2020GL092075 (2021). e2020GL092075.

35. Milovac, J. et al. Investigation of PBL schemes combining the WRF model simulations with scanning water vapor differential absorption lidar measurements. *J. Geophys. Res. : Atmos.* **121**, 624–649. https://doi.org/10.1002/2015JD023927 (2016).

36. Yang, B., Zhang, Y., Qian, Y., Huang, A. & Yan, H. Calibration of a convective parameterization scheme in the WRF model and its impact on the simulation of east Asian summer monsoon precipitation. *Clim. Dyn.* **44**, 1661–1684. https://doi.org/10.1007/s00382-014-2118-4 (2015).

37. Bao, J., Feng, J. & Wang, Y. Dynamical downscaling simulation and future projection of precipitation over China. *J. Geophys. Res. : Atmos.* **120**, 8227–8243. https://doi.org/10.1002/2015JD023275 (2015).

38. Yang, Q. et al. Performance of the WRF model in simulating intense precipitation events over the Hanjiang River Basin, China – A multi-physics ensemble approach. *Atmos. Res.* **248**, 105206. https://doi.org/10.1016/j.atmosres.2020.105206 (2021).

39. Gao, L. et al. Simulation of an Extreme Precipitation Event using ensemble-based WRF model in the Southeastern Coastal Region of China. *Atmosphere* **13**, 194. https://doi.org/10.3390/atmos13020194 (2022).

40. Deng, C. et al. Sensitivity of WRF multiple parameterization schemes to extreme precipitation event over the Poyang Lake Basin of China. *Front. Environ. Sci.* **10**, 1102864. https://doi.org/10.3389/fenvs.2022.1102864 (2023).

41. Skamarock, W. C. et al. n.d. A Description of the Advanced Research WRF Model Version 4 165. https://api.semanticscholar.org/CorpusID:196211930.

42. Lin, S. et al. Sensitivity study of WRF parameterization schemes and initial fields on simulation of rainstorm in the Minjiang River basin. *Pearl River (in Chinese).* **44** (10), 35–46. https://doi.org/10.3969/j.issn.1001-9235.2023.10.004 (2023).

43. Zhang, C., Wang, Y. & Hamilton, K. Improved Representation of Boundary Layer Clouds over the Southeast Pacific in ARW-WRF using a modified Tiedtke Cumulus Parameterization Scheme*. *Mon Weather Rev.* **139**, 3489–3513. https://doi.org/10.1175/MWR-D-10-05091.1 (2011).

44. Chen, S. H. & Sun, W. Y. A one-dimensional time dependent cloud model. *J. Meteorol. Soc. Japan.* **80**, 99–118. https://doi.org/10.2151/jmsj.80.99 (2002).

45. Dudhia, J. Numerical Study of Convection observed during the Winter Monsoon Experiment using a Mesoscale two-Dimensional Model. *J. Atmos. Sci.* **46**, 3077–3107 (1989).

46. Mlawer, E. J., Taubman, S. J., Brown, P. D., Iacono, M. J. & Clough, S. A. Radiative transfer for inhomogeneous atmospheres: RRTM, a validated correlated-k model for the longwave. *J. Geophys. Res. : Atmos.* **102**, 16663–16682. https://doi.org/10.1029/97JD00237 (1997).

47. Chen, F. & Dudhia, J. Coupling an Advanced Land surface–hydrology model with the Penn State–NCAR MM5 modeling system. Part I: model implementation and sensitivity. *Mon Weather Rev.* **129**, 569–585 (2001).

48. Arakawa, A. & Jung, J. H. Multiscale modeling of the moist-convective atmosphere — a review. *Atmos. Res.* **102**, 263–285. https://doi.org/10.1016/j.atmosres.2011.08.009 (2011).

49. Sertel, E., Robock, A. & Ormeci, C. Impacts of land cover data quality on regional climate simulations. *Int. J. Climatol.* **30**, 1942–1953. https://doi.org/10.1002/joc.2036 (2010).

50. Cheng, F. Y., Hsu, Y. C., Lin, P. L. & Lin, T. H. Investigation of the effects of different land use and land cover patterns on Mesoscale Meteorological Simulations in the Taiwan Area. *J. Appl. Meteorol. Clim.* **52**, 570–587. https://doi.org/10.1175/JAMC-D-12-0109.1 (2013).

51. Zha, J., Zhao, D., Wu, J. & Zhang, P. Numerical simulation of the effects of land use and cover change on the near-surface wind speed over Eastern China. *Clim. Dyn.* **53**, 1783–1803. https://doi.org/10.1007/s00382-019-04737-w (2019).

52. Hersbach, H. et al. The ERA5 global reanalysis. *Q. J. Roy Meteor. Soc.* **146**, 1999–2049. https://doi.org/10.1002/qj.3803 (2020).

53. Yin, H. & Sun, Y. Characteristics of extreme temperature and precipitation in China in 2017 based on ETCCDI indices. *Adv. Clim. Chang. Res.* **9**, 218–226. https://doi.org/10.1016/j.accre.2019.01.001 (2018).

54. Lei, X. et al. Does non-stationarity of extreme precipitation exist in the Poyang Lake Basin of China? *J. Hydrol. : Reg. Stud.* **37**, 100920. https://doi.org/10.1016/j.ejrh.2021.100920 (2021).

55. Wang, L. et al. Spatiotemporal variations of extreme precipitation and its potential driving factors in China's North-South Transition Zone during 1960–2017. *Atmos. Res.* **252**, 105429. https://doi.org/10.1016/j.atmosres.2020.105429 (2021).

56. Alexander, L. V. et al. On the use of indices to study extreme precipitation on sub-daily and daily timescales. *Environ. Res. Lett.* **14**, 125008. https://doi.org/10.1088/1748-9326/ab51b6 (2019).

57. Irannezhad, M., Chen, D., Kløve, B. & Moradkhani, H. Analysing the variability and trends of precipitation extremes in Finland and their connection to atmospheric circulation patterns. *Int. J. Climatol.* **37**, 1053–1066. https://doi.org/10.1002/joc.5059 (2017).

58. Yue, S. & Wang, C. Y. Applicability of prewhitening to eliminate the influence of serial correlation on the Mann-Kendall test. *Water Resour. Res.* 38. https://doi.org/10.1029/2001WR000861 (2002).

59. Burn, D. H. & Hag Elnur, M. A. Detection of hydrologic trends and variability. *J. Hydrol.* **255**, 107–122. https://doi.org/10.1016/S0022-1694(01)00514-5 (2002).

60. Hamed, K. H. Enhancing the effectiveness of prewhitening in trend analysis of hydrologic data. *J. Hydrol.* **368**, 143–155. https://doi.org/10.1016/j.jhydrol.2009.01.040 (2009).

61. Xu, W. et al. How well does the ERA5 reanalysis capture the Extreme Climate events over China? Part II: Extreme temperature. *Front. Environ. Sci.* **10**, 921659. https://doi.org/10.3389/fenvs.2022.921659 (2022).

62. Hu, Y. & Ding, Y. The Progress of RCMs Simulation on East Asia Region. *Adv. Earth Sci. (in Chinese).* **21** (9), 956–964. https://doi.org/10.11867/j.issn.1001-8166.2006.09.0956 (2006).

63. Huang, D. & Gao, S. Impact of different reanalysis data on WRF dynamical downscaling over China. *Atmos. Res.* **200**, 25–35. https://doi.org/10.1016/j.atmosres.2017.09.017 (2018).

64. Di, C., Wang, T., Yang, X. & Li, S. Technical note: an improved grassberger–procaccia algorithm for analysis of climate system complexity. *Hydrol. Earth Syst. Sci.* **22**, 5069–5079. https://doi.org/10.5194/hess-22-5069-2018 (2018).

65. Xie, J. et al. Implementation of an Orographic Drag Scheme considering Orographic Anisotropy in all Flow directions in the Earth System Model CAS-ESM 2.0. *J. Adv. Model. Earth Syst.* **13**, e2021MS002585. https://doi.org/10.1029/2021MS002585 (2021).

66. Zou, Y., Wei, Z., Zhan, Q. & Zhou, H. An extreme storm over the Nanling Mountains during Typhoon Bilis and the roles of terrain. *Nat. Hazards.* **116**, 795–815. https://doi.org/10.1007/s11069-022-05699-9 (2023).

67. Norris, J. et al. The spatiotemporal variability of precipitation over the Himalaya: evaluation of one-year WRF model simulation. *Clim. Dyn.* **49**, 2179–2204. https://doi.org/10.1007/s00382-016-3414-y (2017).

68. Musaid, P. P., Manoj, M. G., Panda, S. K., Das, S. & Mohanakumar, K. Dynamical influence of West Pacific typhoons on the 2018 historic flood of Kerala as revealed by the weather research and forecasting (WRF) model. *Clim. Dyn.* **61**, 1663–1681. https://doi.org/10.1007/s00382-022-06648-9 (2023).

69. Cornejo, I. C., Rowe, A. K., Rasmussen, K. L. & DeHart, J. C. Orographic Controls on Extreme Precipitation Associated with a Mei-Yu Front. *Mon Weather Rev.* **152**, 531–551. https://doi.org/10.1175/MWR-D-23-0170.1 (2024).

70. Wang, C., Zeng, Z. & Ying, M. Uncertainty in Tropical Cyclone intensity predictions due to uncertainty in initial conditions. *Adv. Atmos. Sci.* **37**, 278–290. https://doi.org/10.1007/s00376-019-9126-6 (2020).

71. Min, Y., Huang, W., Ma, M. & Zhang, Y. Simulations in the Topography Effects of Tianshan Mountains on an Extreme Precipitation Event in the Ili River Valley, China. *Atmosphere* 12, 750. (2021). https://doi.org/10.3390/atmos12060750
72. Smith, R. B. The influence of Mountains on the atmosphere, in: Adv. Geophys. Elsevier, 87–230. https://doi.org/10.1016/S0065-2687(08)60262-9 (1979).
73. Utsumi, N., Kim, H., Kanae, S. & Oki, T. Relative contributions of weather systems to mean and extreme global precipitation. *J. Geophys. Res. : Atmos.* 122, 152–167. https://doi.org/10.1002/2016JD025222 (2017).
74. Cui, D., Wang, C. & Santisirisomboon, J. Characteristics of extreme precipitation over eastern Asia and its possible connections with Asian summer monsoon activity. *Int. J. Climatol.* 39, 711–723. https://doi.org/10.1002/joc.5837 (2019).
75. Yang, Y., Gao, M., Xie, N. & Gao, Z. Relating anomalous large-scale atmospheric circulation patterns to temperature and precipitation anomalies in the east Asian monsoon region. *Atmos. Res.* 232, 104679. https://doi.org/10.1016/j.atmosres.2019.104679 (2020).
76. Tian, Y., Mcbride, J. L., Ren, F., Li, G. & Feng, T. Changes in Typhoon Regional Heavy precipitation events over China from 1960 to 2018. *Adv. Atmos. Sci.* 39, 272–283. https://doi.org/10.1007/s00376-021-1015-0 (2022).
77. Singh, S., Kumar, N., Goyal, M. K. & Jha, S. Relative influence of ENSO, IOD, and AMO over spatiotemporal variability of hydroclimatic extremes in Narmada basin, India. *AQUA — Water Infrastruct. Ecosyst. Soc.* 72, 520–539. https://doi.org/10.2166/aqua.2023.219 (2023).
78. Mandal, M., Singh, K. S., Balaji, M. & Mohapatra, M. Performance of WRF-ARW model in real-time prediction of Bay of Bengal cyclone 'Phailin'. *Pure Appl. Geophys.* 173, 1783–1801. https://doi.org/10.1007/s00024-015-1206-7 (2016).
79. Qiu, W., Ren, F., Wu, L., Chen, L. & Ding, C. Characteristics of tropical cyclone extreme precipitation and its preliminary causes in Southeast China. *Meteorol. Atmos. Phys.* 131, 613–626. https://doi.org/10.1007/s00703-018-0594-5 (2019).
80. Rajeevan, M. et al. Sensitivity of WRF Cloud microphysics to simulations of a severe thunderstorm event over Southeast India. *Ann. Geophys.* 28, 603–619. https://doi.org/10.5194/angeo-28-603-2010 (2010).
81. Kim, J. H., Shin, D. B. & Kummerow, C. Impacts of a Priori databases using six WRF Microphysics schemes on Passive Microwave Rainfall retrievals. *J. Atmos. Ocean. Technol.* 30, 2367–2381. https://doi.org/10.1175/JTECH-D-12-00261.1 (2013).
82. Cossu, F. & Hocke, K. Influence of microphysical schemes on atmospheric water in the Weather Research and forecasting model. *Geosci. Model. Dev.* 7, 147–160. https://doi.org/10.5194/gmd-7-147-2014 (2014).
83. Li, L., Li, W. & Jin, J. Improvements in WRF simulation skills of southeastern United States summer rainfall: physical parameterization and horizontal resolution. *Clim. Dyn.* 43, 2077–2091. https://doi.org/10.1007/s00382-013-2031-2 (2014).
84. Nguyen-Xuan, T., Qiu, L., Im, E. S., Hur, J. & Shim, K. M. Sensitivity of Summer Precipitation over Korea to Convective Parameterizations in the RegCM4: An Updated Assessment. Adv. Meteorol. 2020, 1–15. (2020). https://doi.org/10.1155/2020/1329071
85. Bopape, M. J. M. et al. Sensitivity of Tropical Cyclone Idai simulations to Cumulus parametrization schemes. *Atmosphere* 12 (932). https://doi.org/10.3390/atmos12080932 (2021).
86. Xu, H. et al. Microphysics affect the sensitivities of rainfall to different horizontal-resolution simulations: evidence from a case study of the Weather Research and forecasting model runs. *Atmos. Res.* 296, 107022. https://doi.org/10.1016/j.atmosres.2023.107022 (2023).
87. Burakowski, E. A. et al. Evaluating the Climate effects of Reforestation in New England using a Weather Research and forecasting (WRF) model Multiphysics Ensemble. *J. Clim.* 29, 5141–5156. https://doi.org/10.1175/JCLI-D-15-0286.1 (2016).
88. He, J. J., Yu, Y., Yu, L. J., Liu, N. & Zhao, S. P. Impacts of uncertainty in land surface information on simulated surface temperature and precipitation over China. *Int. J. Climatol.* 37, 829–847. https://doi.org/10.1002/joc.5041 (2017).
89. Feng, J., Wang, J. & Yan, Z. Impact of anthropogenic heat release on regional climate in three vast urban agglomerations in China. *Adv. Atmos. Sci.* 31, 363–373. https://doi.org/10.1007/s00376-013-3041-z (2014).
90. Lin, C. Y., Chen, W. C., Chang, P. L. & Sheng, Y. F. Impact of the Urban Heat Island Effect on Precipitation over a Complex Geographic Environment in Northern Taiwan. *J. Appl. Meteorol. Climatol.* 50, 339–353. https://doi.org/10.1175/2010JAMC2504.1 (2011).
91. Yang, L. et al. Impact of urbanization on heavy convective precipitation under strong large-scale forcing: a Case Study over the Milwaukee–Lake Michigan Region. *J. Hydrometeorol.* 15, 261–278. https://doi.org/10.1175/JHM-D-13-020.1 (2014).
92. Qian, Y. et al. Urbanization impact on Regional Climate and Extreme Weather: current understanding, uncertainties, and future research directions. *Adv. Atmos. Sci.* 39, 819–860. https://doi.org/10.1007/s00376-021-1371-9 (2022).

Acknowledgements

Author contributions

Y.Z.: investigation, visualization, and writing—original draft. C.D. and W.X.: methodology, validation. Y.Z., L.J., C.J. and X.G.: visualization, supervision, and review. J.W., M.M. and J.P.: contributed to the revision of the manuscript. Y.C. and L.G.: Fund support. All authors reviewed and made substantial contributions to this work and approved it for publication.

Funding

Declarations

Competing interests

The authors declare no competing interests.

Additional information

Supplementary Information The online version contains supplementary material available at https://doi.org/10.1038/s41598-024-84076-x.

Correspondence and requests for materials should be addressed to L.G.

Reprints and permissions information is available at www.nature.com/reprints.